31st Congress of the International Council of the Aeronautical Sciences

Belo Horizonte, Brazil; September 09-14, 2018

DESIGN OF AN INSTRUMENTED STATOR VANE FOR UNSTEADY PRESSURE MEASUREMENTS USING MEMS MICROPHONES

Bernardo Martinez R. Jr.[*], Luciano C. Caldas[*], Rafael G. Cuenca[†], Rudner Lauterjung Q.[‡], Paulo C. Greco Jr.[*]

[*]University of São Paulo, [†]Federal University of Santa Catarina, [‡]Embraer S/A

Keywords: *aeroacoustics, fan noise, instrumentation, spectral analysis, tone-broadband separation*

Abstract

The study of turbofan aeroacoustics has become important in academia and industry as noise from other sources in aircraft have been reduced. Rotor-stator interaction noise, which is generated by the impingement of fan wakes on stator vanes, is considered the most prominent sources within engine noise. The pressure oscillations over these stator vanes have two distinct components: tonal and broadband. Knowledge in broadband component is still incipient and experimental methods can provide insights and data for on-going research. In this work, a instrumented stator vane was designed using recently available technologies, as 3D printing and the use of MEMS microphones, to measure this pressure fluctuations. Phase-averaging and the signal from a hall sensor were used to separate broadband content in time series. Broadband level distribution were analyzed for two span lines of the instrumented stator vane and for a reference microphone located in the inlet antenna. Broadband levels increased with the increase in fan speed and its distribution over these span lines maintained its shape for different speeds. Cross-correlation of the microphones were calculated and showed decay of zero-delay cross-correlation with increase in distance between microphones over the vane. And, finally, the integral length scale, obtained by the integration of zero-delay cross-correlation curve, showed decay with increase in fan speed.

1 Introduction

One of the major trends in aircraft engine design has been the increase in size of the fan stage, an approach that has proven itself effective on achieving desired thrust with lower specific-thrust and reduced noise. Fan aero-acoustics is, nowadays, a topic of strong interest in academia and industry, since this increase in fan diameter and developments in jet aero-acoustics made fan noise sources, both at the inlet and outlet of the engine, become more prominent.

Fan noise is a general concept that comprehends many sources as: fan self-noise, rotor-stator interaction (RSI), tip noise, and so on. Rotor-stator interaction noise is generated by the impingement of fan wakes on stator vanes, creating a strong pressure fluctuation field over them. This has been postulated as one of the most important noise sources during take-off and landing operations of an aircraft, when the fan blade tips are in subsonic condition [1].

Pressure oscillations over these stator vanes have two distinct components: a tonal component whose fluctuations are related to rotation, and a random component whose fluctuations are related to turbulent phenomena. While tonal part is well understood and has already been modeled, broadband knowledge is still incipient and experimental methods can provide insights and data for on-going research.

Measurements of unsteady pressure over sta-

tor vanes are scarce in literature. Mueller [2] has published results of stator-vane fluctuating pressures for both static and flight tests. Others studies, at NASA's Advanced Noise Control Fan (ANCF), Sutliff compared the duct modes power level results measured by his rotating rake at the fan inlet and exhaust with what would be obtained by getting the surface pressure on the stator vane and using Green's functions model to predict the noise, finding good prediction accuracy [3]. At NASA's Source Diagnostic Test (SDT), Envia separated the blade passing frequency and broadband contents of the signal obtained and found correlations of the tip speed and the increase in broadband level and indications of broadband homogeneity [1].

The research mentioned above use Kulite pressure sensors for measuring unsteady pressure in such a confined space, although they are worth their value, these sensors have prohibiting prices. Other types of transducer or measurement methods can be used, as, for instance, hot-film anemometry or pressure sensitive paint. Nevertheless, measurements taken using microphones are straightforward and, in this work we propose the use of Micro-Electro-Mechanical Systems (MEMS) microphones.

Advancements in telecommunication industry and the search for small and cheap electronics that have their use widely spread affected many other research areas. With large scale production, these miniaturized microphones became accessible

Fig. 1 The EESC-USP Fan Rig, an aeroacoustic wind tunnel for fan noise measurements.

2 Experimental Setup

2.1 EESC-USP Fan Rig

The tests were ran at the EESC-USP Fan Rig located at the Department of Aeronautical Engineering of the São Carlos School of Engineering. The EESC-USP Fan Rig is a test facility to investigate fan noise sources at the University of São Paulo (Figure 1). The facility provides a flexible configuration that allows changes in operational conditions of the rig. This parameters control tries to isolate the sources as much as possible and analyze each of them individually. Aiming to further investigate the rotor-stator interaction source contribution to overall fan noise, an instrumented vane is being built to record time histories of fluctuating pressures on suction side of one of the vanes on the stator ring.

The fan-stator geometry reproduces one of ANCF's configurations. The configuration reproduced is the one with 16 blades and 14 vanes. The fan and stator diameters are 500 mm and the hub diameter is 200 mm. As consequence, vanes and blades spans are 150 mm. Also, blade mean chord is 50 mm, and stator vanes constant chord is 46 mm.

In this set of experiments, rotor-stator spacing was maintained constant and equal to 0.5 blade chords, from trailing edge of blade to leading edge of vane in mean stage radius. Fan speeds were tested from 2000 to 4500 rpm, in 250 rpm steps, and no throttling was applied in duct outlet.

2.2 Measurement Systems

Measurements were taken from two sources: an antenna array of microphones mounted in the inlet of the duct, and the microphones embedded in one of the stator vanes. This data were acquired simultaneously at a sampling rate of 102.4 kHz using a NI PXI-1042Q chassis and NI 4496 and NI 4498 data acquisition modules. Each of the tests had the duration of 10 seconds, which corresponds to nearly 330 fan revolutions for the lower speeds and 700 for the higher speeds tested.

An antenna of microphones - disposed in three circumferential rings - was used to capture

the sound pressure in the duct walls upstream to the fan and the full description of this system can be seen in [4] and [5]. This sound pressure levels were taken for comparing with broadband levels of the microphones in the instrumented vane. Although many antenna microphones were used in the experiments, a single one was enough to evaluate the difference in levels due to the distance from the noise sources.

2.2.1 Instrumented Stator Vane

The instrumented stator vane used in this work was designed using recently available technologies, as fused deposition modeling (FDM), 3D printing and the use of MEMS microphones. In this section some considerations regarding the use of these methods is discussed.

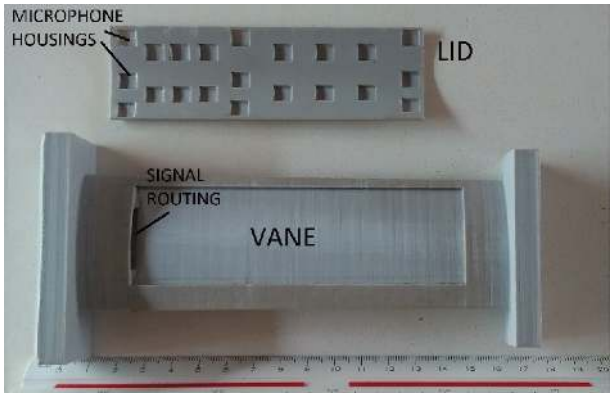

Fig. 2 Manufactured parts of the stator vane using FDM (fused deposition modeling) 3D printing.

The vane was designed in two parts, the main body and a lid, that can be seen in Figure 2. The body follows the design of a regular vane used in the stator assembly, but has a dug area to embed a flexible circuit board (FCB) in which surface mounted microphones are soldered; the signals from the microphones are routed out of the vane via the FCB through a hole which leads to the outer side of the wind tunnel. The lid has small cavities to accommodate the MEMS microphones and fit the dug area in the main body. After lodging the FCB in the vane main body, the lid was positioned and closed. A layer of epoxy resin was added and surface finishing was accomplished by sandpapering. Finally, the vane was painted and holes were pierced in it so that they match the position of the MEMS cavities (final assembly can be seen in Figure 3).

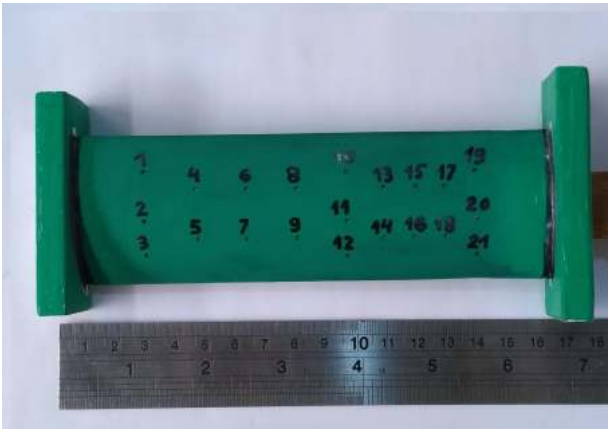

Fig. 3 Final assembly of the stator vane, after surface finishing, and microphones enumeration.

The choice for using MEMS microphones was due to two main factors. First, in this device there is a strong need for small sized transducers, which reduces the range of available sensors. MEMS microphones can be as small as 2.5x3.5x1.5 mm, which make them suitable for this need. Secondly, comparing to other options, they are inexpensive, disposable, electronic components which allow for higher risks in design in such confined space. Furthermore, MEMS microphones are easy to find and optimized for human audible frequencies. On the other hand, when using this type of transducers, it is necessary to design an interface circuit and their calibration is not as straightforward as off-the-shelf microphones, since they do not have a broad flat free field response. Also,comparatively, MEMS microphones have lower acoustic overload point (AOP) and signal-to-noise ratio (SNR).

In our experiment, the frequency range of interest is from 200 to 10 kHz and the maximum SPL is lesser than 120 dB and the chosen MEMS microphone was the SPM0406HE3H-SB [6]. This is a miniature, high performance, low power microphone. Its typical free field response normalized to 1 kHz stays within ± 1 dB from

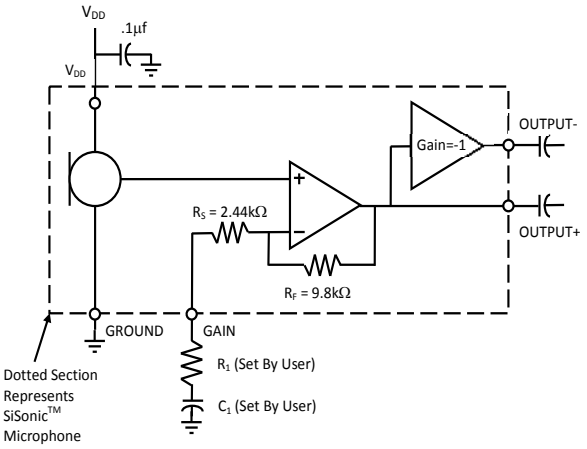

Fig. 4 Circuit scheme for each microphone. Image from product datasheet [6]

200 to 6 kHz and within ±3 dB from 100 to 10 kHz. Its sensitivity is within -25 and -19 dBV/Pa, the total harmonic distortion (THD) is 1% and its signal-to-noise ratio is 59 dB(A-weighted) at 1 kHz and sound pressure level (SPL) of 94 dB. At 1 kHz, limiting to 10% THD, supplying 5.5V and using 0 dB gain, the minimum acoustic overload point is 115 dB, therefore this microphone corresponds to the needs. Also, the maximum thickness acceptable should not be greater than 2mm and this microphone is only 1.25mm thick.

The circuit board was designed and manufactured in-house, following instructions of the design guide and datasheet provided by the MEMS microphone manufacturer. The electronics design was set to have no gain, in order to have maximum acoustic overload point (AOP), delaying as much as possible saturation of the transducer signal. The circuit scheme used for each microphone is shown in Figure 4, it consists of an energy supply, V_{DD}, for the microphones which was set to $5\,V$DC, a filtering capacitor, surface mounted (SMD), put next to the MEMS ($0.1\,\mu F$). Microphone signal was routed single-ended to the acquisition board using OUTPUT+ pin and connecting it to pin GAIN, without using R_1 and C_1, so that the gain was set to 0 dB. Pin OUTPUT- was ignored. This block was reproduced for the 21 microphones, and then it was printed in a flexible circuit board which was later corroded. The SMD components (the microphones and filtering capacitors) were soldered with the use of a reflow oven and the final result can be seen in Figure 5. The profile of temperatures was taken from the design manual of the MEMS microphone.

Fig. 5 Embedded circuit board mounted within the stator vane.

Finally, for this tests a *in loci* calibration method was done using an NC-74 RION Sound Calibrator and putting its tube in touch with the vane surface after the installation of the MEMS microphones within it.

3 Data Processing

3.1 Spectral and Correlation Analysis

A standard way to characterize aeroacoustic measurements is throughout their power spectral density. As input, for each configuration, a sampling frequency of 102.4 kHz and 10 seconds of acquired acoustic data is used, which allows the adequate use of the well-known Welch's method, with 8192 samples Hanning window and 50% overlap. Plots are displayed in terms of SPL levels by taking the logarithmic value with reference to $p_0 = 20\,\mu Pa$ sound pressure, i.e., $SPL = 10log_{10}(S/p_0^2)$, where S is the power spectrum density estimated. Figure 6 presents an example of spectra obtained at symmetrical locations in the antenna array but using two different types of microphones (MEMS and B&K Microphone Type 4958).

3.2 Tone and Broadband Separation

Figure 7 compares the spectra of two microphones, one, a B&K Microphone Type 4958,

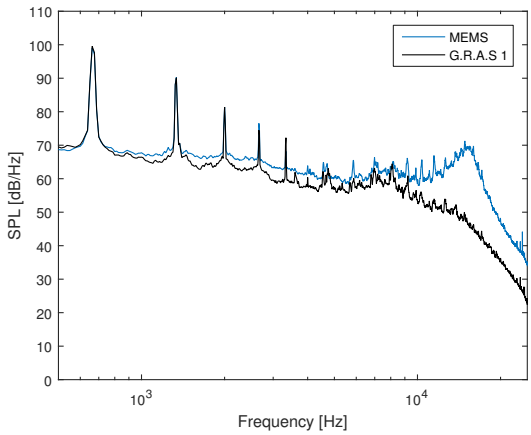

Fig. 6 Comparison of spectra of two microphones mounted in the antenna array (duct inlet): in blue the spectrum from a MEMS microphone and, in black, from a B&K Microphone Type4958.

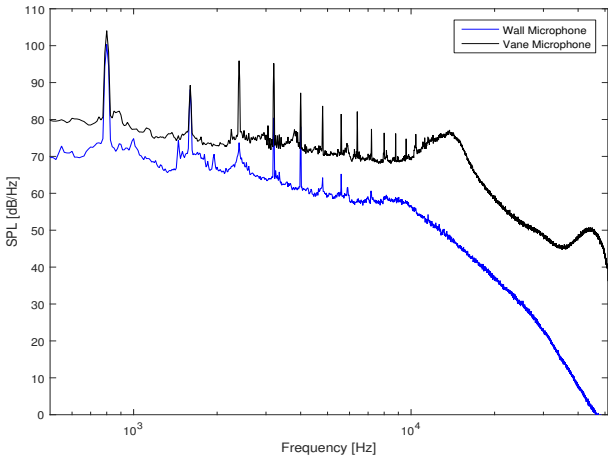

Fig. 7 Comparison of spectra from a MEMS microphone in the stator vane (in black) and from a B&K Microphone Type4958 (in blue) mounted in the antenna array (duct inlet).

mounted in the antenna array and one, a MEMS microphone, within the stator vane. Obviously, as the vane microphone is much closer to the noise sources, the power level is higher and the spectrum appears shifted up. Also, there are some amplification effects present in the spectrum of the vanes microphones at frequencies higher than 10 kHz. The first bump (from 10 to 20 kHz) is due to a cavity effect (Helmholtz cavity) due to the fact that MEMS microphones have a housing to the sensing membrane. The second bump should have a similar explanation but no literature was found in this effect.

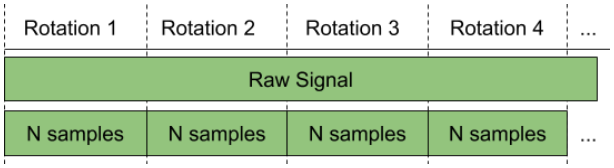

Fig. 8 Segment cutting process for phase-averaging method without signal alignment.

To separate the tonal content from the signal obtained at any given experiment, one can phase-average it. To do so, the signal should be cut in to a set of samples with the size of a rotor revolution (as shown in Figure 8). This task is not straightforward, because it would result in sets of samples containing the periodic data, as shown in Figure 9, which are not aligned. As these sets need to be summed up and then divided by the revolutions count, this unalignment would cause the average to fail and tend to zero. This data unalignment is caused by jitter (time intervals between samples can have small differences and the rotor speed is not exactly constant, i.e. it can drift) and this should be assessed in order to properly sum the data and divide by the number of revolutions, while accounting for all tonal content.

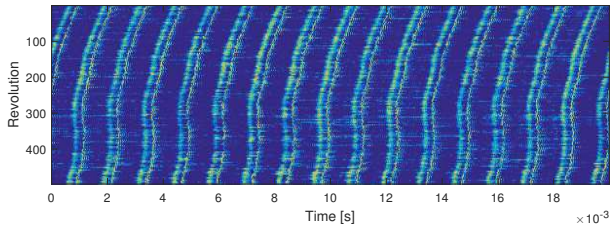

Fig. 9 Raw signal (i.e. unaligned) time series. The x-axis is limited to the number of samples corresponding to a fan rotation. Each of the the stripes show the pressure peak from a blade passage (16 per rotation, same number as blade counting).

To measure this jitter effect and mitigate its effect on the averaging, a Hall effect sensor was used with a magnet glued to the shaft. Raw data

from this sensor consists of square signals corresponding to the magnet passage by the sensor. This data is processed by transforming into one-zero signal with one being exactly the moment when the signal change from low to high value as exemplified by Figure 10. This allows to count the number of samples that correspond to each revolution of the fan.

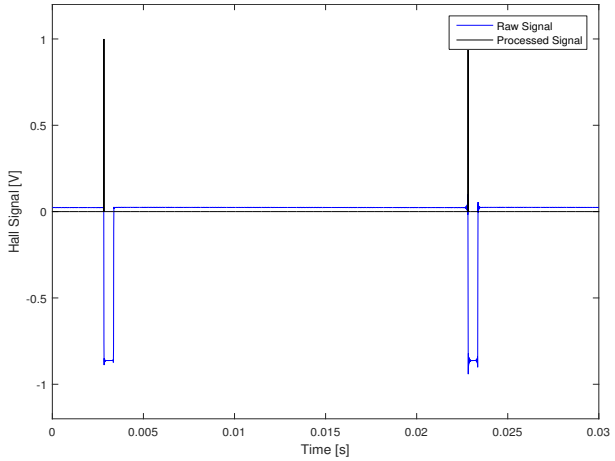

Fig. 10 Processing hall signal. In blue, the raw signal is measured as a step signal, every time the rotor completes a full rotation. In black, the signal is transformed into a pulse signal.

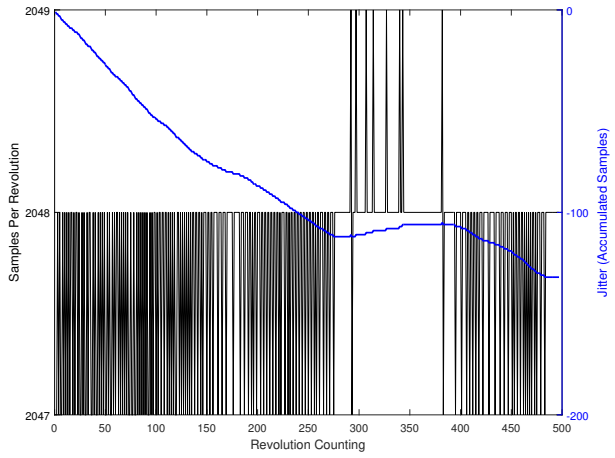

Fig. 11 The difference, in samples, between the pulses in processed sensor hall signal is counted and shown in black for each individual revolution. The accumulated sum of the difference the measured and averaged samples per revolution, known as jitter, is plotted in blue.

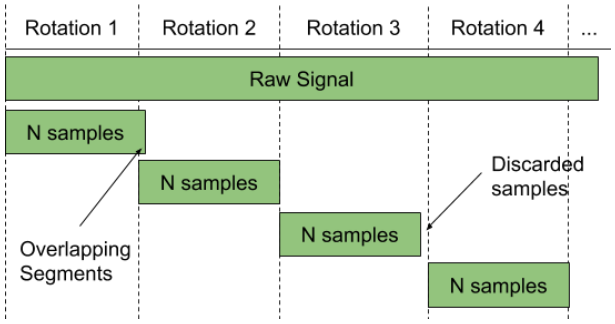

Fig. 12 Segment cutting process for phase-averaging method using processed hall sensor signal for microphones signal alignment.

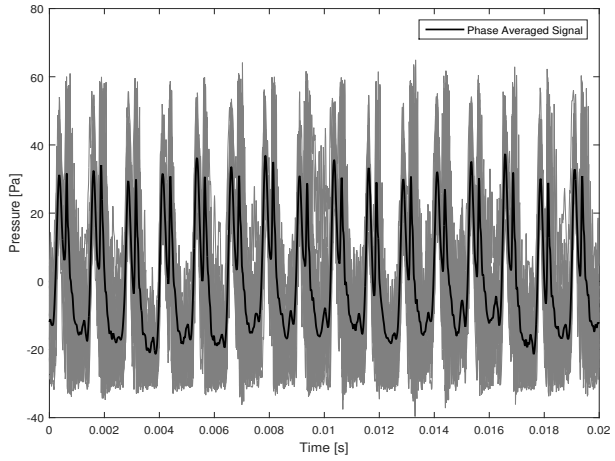

Fig. 13 Phase-averaging the signal. In gray the signals from all revolution are superposed and, in black, their average is shown.

The number of samples corresponding to each revolution and the accumulated jitter over one experiment acquisition is shown in Figure 11. It is possible to see that the number of samples per revolution (SPR) oscillates between 2047 and 2049, being 2048 the expected value. The segment cutting process using the processed Hall sensor signal is shown in Figure 12: if the SPR is lower than expected, the missing sample needs to be borrowed from the next interval. Alternatively, if it is higher, the extra sample needs to be discarded. By doing this, one can obtain the aligned sets of data and average them out to obtain the periodic phase-averaged time series, as seen in Figure 13. Figure 14 shows the aligned raw signal and its broadband component, which is obtained by subtracting the periodic phase-

averaged signal from the raw signal.

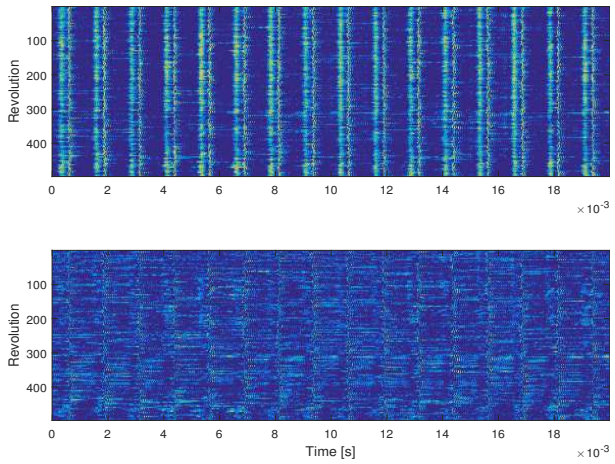

Fig. 14 Microphones signals time series after alignment. The x-axis is limited to the number of samples corresponding to a fan rotation. Each of the the stripes show the pressure peak from a blade passage (16 per rotation, same number as blade counting). Upper image shows complete (tonal + broadband signal) and lower image shows the time series after removal of periodic signal.

Figure 15 shows the spectral separation process. The upper graph shows the spectrum of the total signal (both coherent and incoherent components). The center graph shows the division in two components, in black, the periodic part - coherent to rotor revolutions - and, in blue, the broadband component - incoherent. It is possible to double check that the broadband hump do not contain periodic signal by increasing the refinement in the frequency discretization and checking if the power associated with the BPF frequency does not increase.. The lower graph shows the extraction of BPF spectrum: in it the periodic component, which contain noise generation related both to blade passages and blade-to-blade differences, is phase-averaged once again, to the period of one blade passage, and the BPF spectrum is then extracted.

4 Broadband Results

After the spectral separation into broadband and tonal components is done, broadband levels can

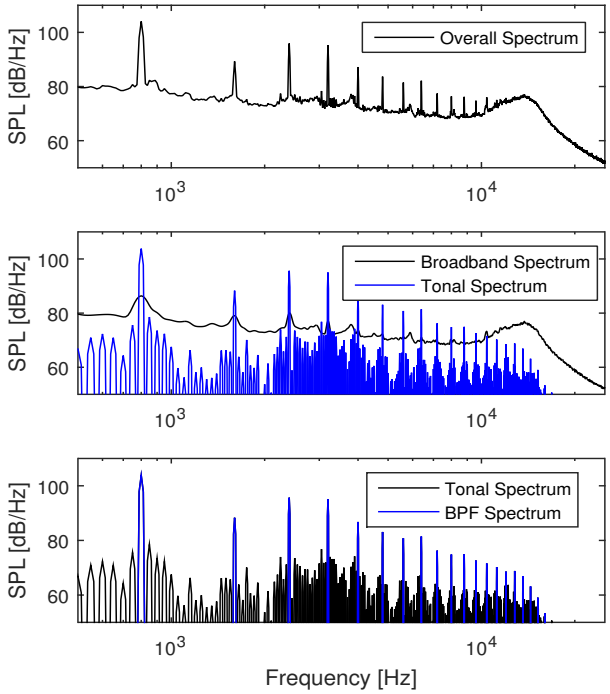

Fig. 15 Spectral separation. First image (up) shows the complete spectrum of a measurement. Second image (center) shows the separation of the spectrum into two parts, broadband and tonal spectra. Third image (down) shows the tonal and BPF spectra (this last is obtained by performing a second phase-averaging procedure).

be analyzed separately. In this work, these levels are condensed into a single value by integrating the spectra from 10 Hz - to avoid low frequency noise contamination due to limited acquisition time - to 12 kHz - which allows capturing overall trend but avoids considering the cavity resonance effect, present in high frequencies. For this analysis a wall-mounted microphone, installed at the inlet antenna, and two span lines are considered (at 30% and 63% chord).

The analysis firstly uses the spectra of the microphones in order to observe the effect of the rotational speed on the averaged levels and its distribution over the vane. Later, data time-series is used to observe the effect of rotational speed on zero-delay cross-correlation coefficients and integral lengthscale for the microphones distributed over the mentioned span lines.

Figure 16 shows the effect of the increase in fan speed in the averaged level over the vane and for a wall mounted microphone. It is possible to see a trend of increasing level with fan speed, but for higher speeds the increase amount diminishes for the vane microphones. This could be a physical limitation of the transducer, i.e. acoustic overload point could have been reached, since the trend does not change for the wall mounted microphone.

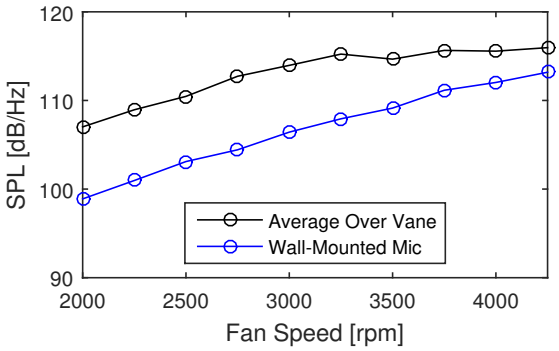

Fig. 16 Effect of fan tip speed for average broadband level in vane MEMS microphones and in inlet wall-mounted microphone.

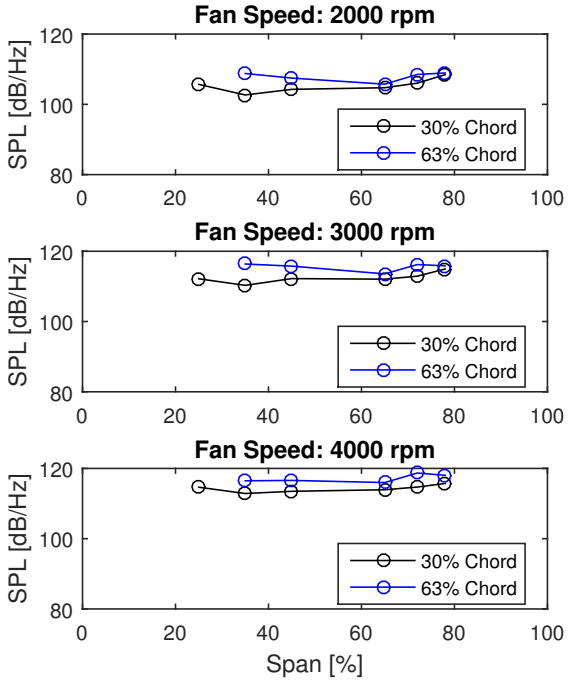

Fig. 17 Distribution of integrated broadband level for microphones over two span lines and three different fan speeds.

Figure 17 shows the distribution of the integrated broadband level for two span lines (at 30% and 60% chords) and for three fan speeds. It is possible to see that the distribution is almost flat over the vane, with a levels little lower mid-vane. Also, as in Figure 16, it is possible to observe that the levels increase with speed, the new information is that the shape of distribution maintains itself for all three speeds.

Figure 18 shows the correlation coefficient comparing multiple microphones along a span line. The coefficient $\rho_{(i,j)}$ corresponds to the cross-correlation between microphones i and j according to the delay of the signals in samples (function *xcorr()* in Matlab). The figure shows that the farther apart microphones are from each other, the lower is the value of the zero-delay correlation coefficient (peak value in the center of the graphs). As expected, the peak value is reduced with greater spacing, because broadband pressure oscillations are localized and have small wavenumber. The presence of the peak near zero delay also indicates that this is a acoustic phenomenon, i.e. its information speed is greater than flow speed. Figure 19 shows the levels of the mentioned peaks, i.e. zero-delay correlation coefficient value, reducing as the microphones distance grows and also that the as the speed is increased, the curve is shifted down and correlation disappears for smaller distances.

Figure 20 shows the effect of increasing the fan speed in the integral length scale. The integral length scale is obtained by integrating the zero-delay coefficient up to the distance where it loses the correlation completely (i.e. becomes nearly zero). In here, this integration was obtained by calculating the area below the curves that better fit the points. In this best fit calculation a bi-gaussian function with zero means was used, so that the curves ares represented by two standard deviation values.

Two different span lines and the microphones along them were considered and compared. The trend lines make clear the decrease of lengthscale

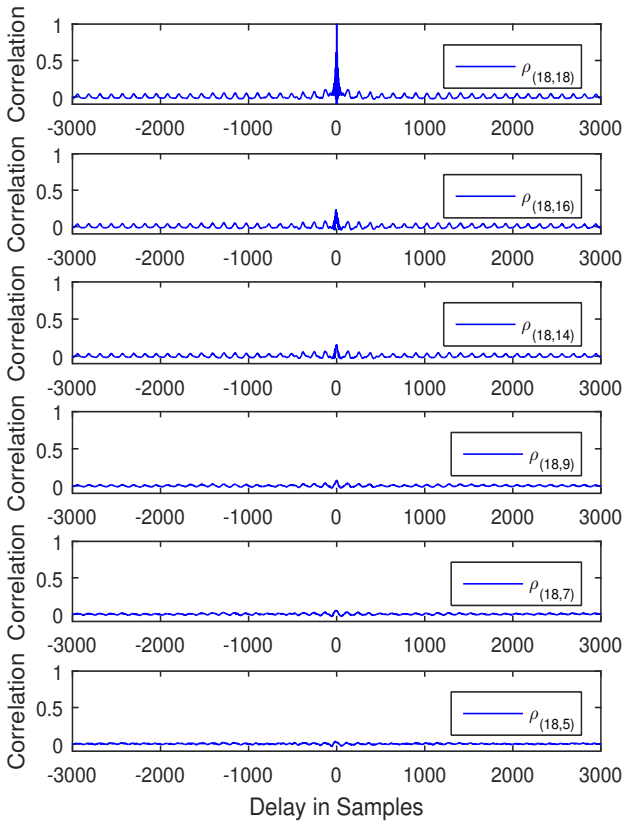

Fig. 18 Auto-correlation and cross-correlation comparing the signals from microphone 18 and microphones distributed over its span line (itself and microphones 16, 14, 9, 7, and 5).

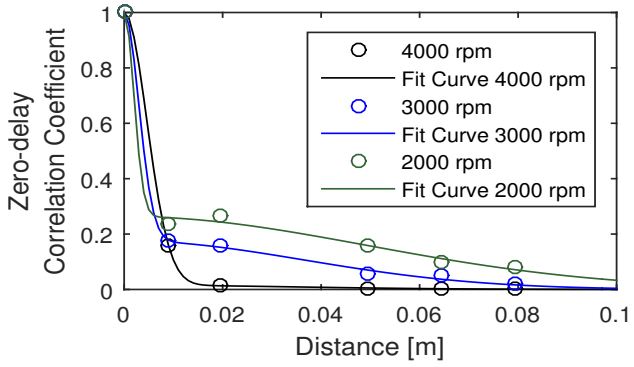

Fig. 19 Zero-delay auto-correlation and cross-correlation comparing the signals from microphone 18 and microphones distributed over its span line (itself and microphones 16, 14, 9, 7, and 5) for three different fan speeds.

with the increase in fan speed, just as shown in last figure and what was observed in the experiments of reference [1]. In this reference article, a homogeneous pressure field is also hypothesized from the little difference between the spatial coherence in spanwise and chordwise directions. Here, the deviation of the data points from the fit curves makes it possible to believe that both curves are close enough to indicate homogeneity spanwise as well. Nevertheless, more data in different directions should be assessed to better support this evidence.

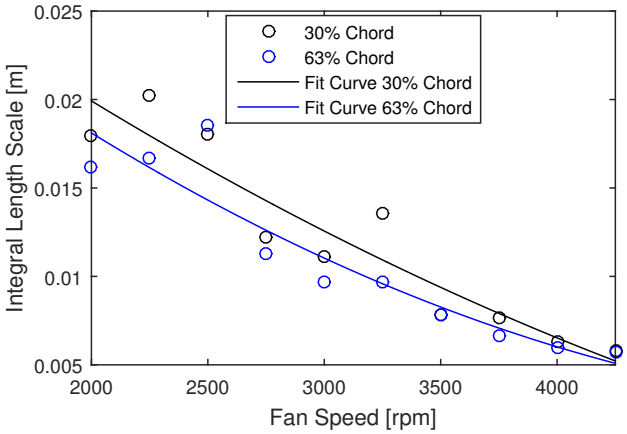

Fig. 20 Effect of fan tip speed in pressure integral length scales, which are obtained by integrating the fit curves from zero-delay correlation coefficient over two span lines (at 30 and 63% chord).

5 Conclusion

In this work, the use of MEMS microphones was proposed as an alternative fan noise aeroacoustic measurements sensor. A measurement device was designed and manufactured to achieve this goal. The chosen MEMS microphones provide an almost flat response in the frequency bands of interest and were calibrated *in loci* using an appropriate calibrator.The measured signals were processed in order to separate tonal and broadband components using a hall sensor signal and phase-averaging technique. Measurement results obtained using MEMS microphones were compatible to more expensive alternatives even without multi-frequency calibration. The drawback

is that for high fan speeds, as the pressure oscillations are too high, the acoustic overload point might have been reached as the broadband levels stop increasing, indicating transducer saturation. Broadband level distribution were measured in two span lines of the instrumented stator vane and in one of the antenna microphones. It was possible to notice that the broadband levels increased with the increase in fan speed and that its distribution over these span lines maintained its shape for different speeds. Cross-correlation of the microphones were calculated and showed decay of zero-delay cross-correlation with increase in distance between microphones. The integral length scale, obtained by the integration of zero-delay cross-correlation curve, showed decay with increase in fan speed and both span lines presented similar values of the integral length scale, indicating broadband homogeneity span-wise. These results come to contribute to the understanding of the broadband noise generated by rotor-stator interaction in turbofan engines.

Acknowledgements

The EESC-USP Fan Rig was financially supported by FINEP (Studies and Projects Financing Agency) and was designed, manufactured and assembled with the help of the technicians and engineers of the School of Engineering of São Carlos (USP) and with the Embraer's engineering team cooperation. Special thanks to Prof. Catalano, and the technicians Mario Sbampato, Fabio Gallo, Claudio Azevedo and Osnan Faria whose help was fundamental to the development of this work. This work is part of Embraer's Silence Research Project.

References

[1] Envia, E. Fan Noise Source Diagnostics Test - Vane Unsteady Pressure Results. *8th AIAA/CEAS Aeroacoustics Conference and Exhibit*, Breckenridge, CO, USA, 2002.

[2] Mueller, W. Study of stator-vane fluctuating pressures in a turbofan engine for static and flight tests *NASA Technical Report TP-2217*, NASA Langley Research Center; Hampton, VA, USA, 1984.

[3] Sutliff, D; Heidelberg, L and Envia E. Coupling of low speed fan stator vane unsteady pressures to duct modes - Measured vs. predicted. *5th AIAA/CEAS Aeroacoustics Conference and Exhibit*, Bellevue, WA, USA, 1999.

[4] Martinez, B, et al. Baseline Acoustic Levels of the EESC-USP Fan Rig. *23rd AIAA/CEAS Aeroacoustics Conference*, Denver, CO, USA, 2017.

[5] Caldas, L. In-duct beamforming and mode detection using a circular microphone array for the characterisation of broadband aeroengine fan noise. *Master's dissertation.* Universidade de São Paulo, 2016.

[6] Acoustics, Knowles. SPM0406HE3H-SB - Differential SiSonicTM Microphone With Enhanced RF Protection *Product Datasheet Rev. E*, 2013.

[7] Sree, D. A novel signal processing technique for separating tonal and broadband noise components from counter-rotating open-rotor acoustic data. *International Journal of Aeroacoustics*, Vol. 12, No. 1-2, pp 169-188, 2013.

6 Contact Author Email Address

For any inquiries or questions regarding the contents of this paper please contact the authors in: bernardo.rocamora@usp.br (Martinez, Bernardo), pgreco@sc.usp.br (Greco, Paulo), rafael.cuenca@ufsc.br (Cuenca, Rafael) and luciano.caldas@usp.br (Caldas, Luciano).

Copyright Statement